

Modeling Sea Ice Thickness using Machine Learning and Remote Sensing Modalities

John Baker

Ira A. Fulton Schools of Engineering

School of Computing and Augmented Intelligence

APPROVED:

Dr. Douglas Cochran _____, Director

Dr. Hua Wei _____, Second Reader

ACCEPTED:

Dean, Barrett, the Honors College

ARIZONA STATE UNIVERSITY

Modeling Sea Ice Thickness using
Machine Learning and Remote
Sensing Modalities

HONORS THESIS
BARRETT, THE HONORS COLLEGE

Author:
John Baker

Committee:
Dr. Douglas Cochran
Dr. Hua Wei

April 2024

Acknowledgement

I would like to thank my director, Dr. Douglas Cochran, and committee member, Dr. Hua Wei, for their support in pursuing this undergraduate research opportunity. Additionally, I'd like to acknowledge the European Space Agency for their sponsorship of the data curated for this study. This work was supported in part by the Office of the Secretary of Defense Multi-disciplinary University Research Initiative (MURI) under ONR Grant No. N00014-20-1-2595.

Abstract

Little is known about the state of Arctic sea ice at any given instance in time. The harshness of the Arctic naturally limits the amount of in-situ data that can be collected, resulting in gathered data being limited in both location and time. Remote sensing modalities such as satellite Synthetic Aperture Radar (SAR) imaging and laser altimetry help compensate for the lack of data, but suffer from uncertainty because of its inherent indirectness. Furthermore, precise remote sensing modalities tend to be severely limited in spatial and temporal availability, while broad methods are more accessible at the expense of precision. This thesis focuses on the intersection of these two problems and explores the possibility of corroborating remote sensing methods to create a precise, accessible source of data that can be used to examine sea ice at a local scale.

Contents

1	Introduction	4
2	Data Collection	9
2.1	SAR Imaging	9
2.2	Laser Altimetry (IceSat-2)	11
3	Experimentation	14
3.1	Setup	14
3.2	Model Results	16
4	Discussion	18
4.1	Technical Limitations	18
4.2	Conceptual Limitations	19
4.3	Practical Implications	21
4.4	Future Work	22
5	Conclusion	23
List of Figures		24
A	Appendix A: ATL10 Product	i

Introduction

In recent decades, understanding the state of sea ice has grown increasingly important. Sea ice analysis at large scales can provide valuable insight into the trajectory of climate change and at local scale has implications in fields like arctic navigation. Understanding sea-ice thickness in particular, is important for both of these applications. For example, the thickness of the ice can be analyzed over time to track ice mass in relation to global warning or interpreted locally to predict shipping speed through ice-covered water [1].

Due to the harsh nature of the arctic, in-situ studies of arctic ice are infrequent both in time and space. Thus, most analyses depend heavily on remote sensing methods. These methods cumulatively provide magnitudes more data than in-situ measurements can achieve, but differ in modality, methodology and resolution. Satellite Synthetic Aperture Radar (SAR) and light detection and ranging (LiDAR) are some such modalities that survey the arctic region.

Organizations like the National Aeronautics and Space Administration (NASA) and European Space Agency (ESA) freely provide this information through their constellation of satellites.

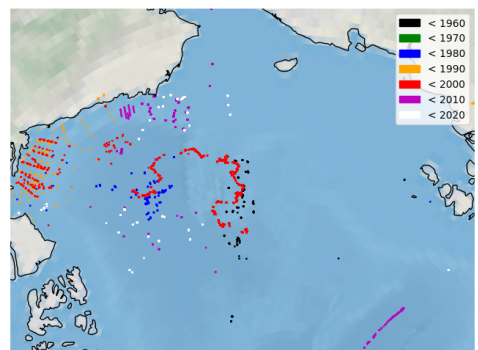


Figure 1.1: Historic In-Situ Data Availability in the Beaufort Sea Region

Each of these remote sensing methods have their individual strengths and limitations. ICESat-2 (IS-2), a NASA LiDAR satellite, features 6 separate lasers and works by emitting individual photons and timing their respective returns. Praised for its precision, its readings are statistically corrected to adjust for ambient light, cloud occlusion (atmospheric scattering), snow and ice scattering, and the physical problem of first-photon bias [2]. Its lasers have a ground-surface footprint of 17 meters, demonstrating how local its sampling is. IS-2's statistical robustness offers valuable local observation with less than 5 meters of total geolocation error (mean $+1\sigma$) [3].

In contrast to IS-2's highly accurate and local measurements, SAR imaging offers significantly more expansive data with a loss in local precision. SAR images Earth's surface by emitting radio waves and then reconstructing the surface composition based upon the return signal. The physical difference between photons and radio waves means that LiDAR's limitations with occlusion are actually imperceptible to SAR satellites. Radio waves permeate clouds and snow, and the reconstructed image is independent of light [4]. These weather independent properties make SAR an excellent modality to monitor sea ice especially during winter seasons, with satellites like Sentinel-2 (SN-2) from the ESA offering 290 kilometer swaths of imaging, at resolutions ranging between 10 and 60 meters [5]. It's important to note that despite its extensiveness, SAR is more sensitive to physical factors like surface roughness, slant, and type, and also suffers from speckle noise (Figure 1.2) [4].

Given the availability of remote sensed data and their different observed properties, there is much to be learned about the state of the sea ice by corroborating these data sources with each other. Uniquely, the corroboration of a SAR image with precise LiDAR measurements suggests the possibility of developing a convolutional neural network (CNN) to accurately predict

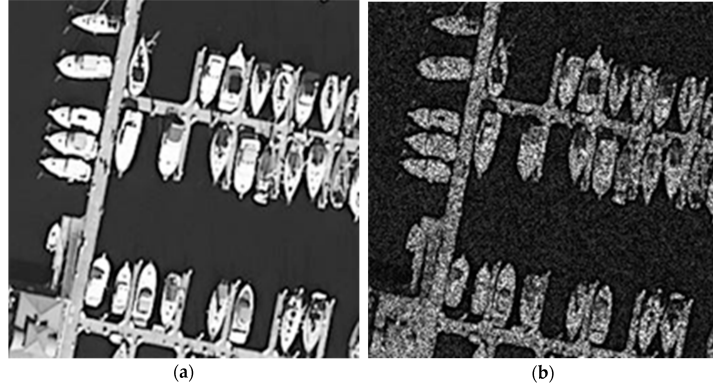


Figure 1.2: (a) Optical Image; (b) SAR Image with speckle noise
[6]

sea ice thickness using expansive SAR imaging. Doing so successfully would effectively map IS-2's precision onto the weather agnostic, extensive imaging gathered by SAR satellites, thus allowing for local scale analysis of sea ice across large regions.

Given that ice thickness is not a property directly measured by LiDAR nor captured in SAR imagery, sets of assumptions need to be made to deduce the property through related measurements. A leading paradigm in modeling ice thickness is through the assumption of hydrostatic equilibrium [7]–[9], in which the properties of the ice sheet are deduced based upon the fact that the ice is buoyant in sea water (Figure 1.3). In this assumption, LiDAR measurements retrieve the elevations of the snow covered ice-surface in relation to the sea surface, and statistically infer the sea ice surface height. It's possible to relate the ice's total thickness to these elevation measurements by combining these relative heights with their associated substance densities (Equation 1.1). NASA's IS-2 L4 Along-Track Sea Ice Thickness product is a closely related example of this topic, and produced arctic ice thickness results between October 2018 and May 2022 [7].

Major critiques of the hydrostatic model stem from its assumption of

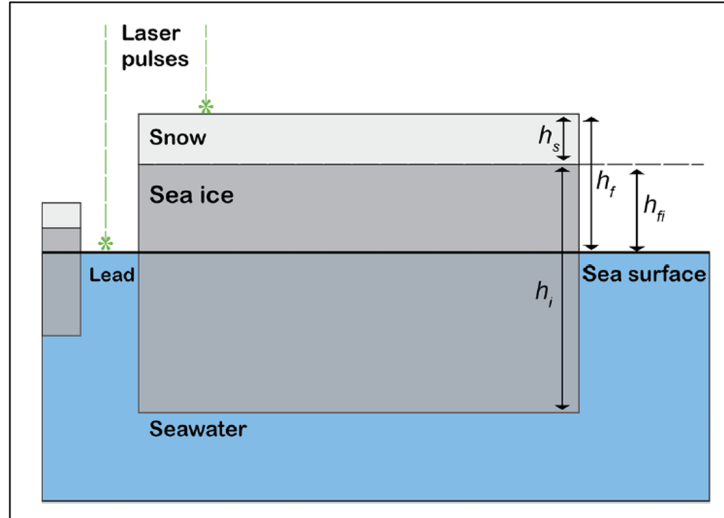


Figure 1.3: Ice Thickness Isostatic Assumption
[7]

the innately variable densities of snow and ice. Ice density is dependent on factors like salinity, temperature, air volume and exposure [1] which all vary across local scales. The differences in ice quality are significant enough that SAR imaging is already capable of segmenting images into their first and multi-year components [10]. Some studies delineate ice density by whether it's above or below the waterline, but find that air-rich above water ice only contributes to 10% of the total density of the ice sheet. Given the variability, the exact local density of sea ice in the remote arctic is ephemeral, but generally agreed upon to be between $900\text{-}940 \frac{kg}{m^3}$, with some studies proposing a slightly wider range of 892-945 [1]. As concrete examples for density though, IS-2's L4 product settled to use a value of $916 \frac{kg}{m^3}$ for ice above and below the waterline and $1024 \frac{kg}{m^3}$ for sea water. Arctic snow density differs from ice density as it is more uniform across the arctic, but varies seasonally across the winter and summer months [11]. Reasonable values range between $210 \frac{kg}{m^3}$ in August, to $350 \frac{kg}{m^3}$ in June [11].

$$h_i = \frac{h_f \rho_w}{(\rho_w - \rho_i)} + \frac{h_s (\rho_s - \rho_w)}{(\rho_w - \rho_i)} \quad (1.1)$$

where:

$$\begin{aligned} h_i &= \text{Sea ice thickness (m)} & \rho_i &= \text{Density of sea ice } (900 - 940 \frac{kg}{m^3}) \\ h_s &= \text{Snow depth (m)} & \rho_s &= \text{Density of snow } (210 - 310 \frac{kg}{m^3}) \\ h_f &= \text{Freeboard height (m)} & \rho_w &= \text{Density of water } (1024 \frac{kg}{m^3}) \end{aligned}$$

Even with the established hydrostatic model in place to infer sea ice thickness from remote sensing methods, there is an innate problem with the corroboration of SAR and LiDAR. IS-2 has an orbit cycle of 91 days, meaning each location is surveyed only once nearly every 3 months [2], while SN-2 orbits nearly once every 5 days [12]. It may appear that there should be plenty of data available given the semi-frequent opportunity for coincidence, but given SN-2's best resolution of 10m, any correlation with IS-2's 17m footprint leads to single pixels of information.

The remainder of the thesis will be split between discussing the data collection and machine learning model experimentation. The data collection section will discuss the procedure for obtaining datasets of interest, as well as some intermediate efforts done to promote accuracy. The experimentation will use the collected data to develop a CNN to explore the feasibility of using such a source of data for deep learning models.

Data Collection

The data collection portion of this project is immediately tasked with the following set of problems: spatial coincidence, temporal coincidence, and resolution. Given the asynchronous orbits of each satellite and the incompatible resolutions of ESA’s SN-2 and NASA’s IS-2, other avenues were explored to obtain precise SAR imaging. Of note were NASA’s ”ICESAT-2” mobile application and ICEYE’s[©] SAR imaging offered through the ESA. The ICESAT-2 mobile application tracks IS-2’s footprint location and lists the dates and times of when the satellite will next fly over a position. ICEYE is a third party satellite provider through the ESA that offers ”SPOT” and ”SLEA” SAR imaging products, featuring 1m resolution and extent ranging from 1km^2 to 15km^2 [13]. The appeal of ICEYE’s 1m resolution products is that a nominal acquisition of its SPOT data product would coincide with ≈ 350 unique IS-2 footprints while the SLEA product would coincide with ≈ 5300 .

2.1 SAR Imaging

ICEYE’s superior resolution is significantly more compatible with IS-2’s small footprint, but is not made freely available as it’s a private company. However, they are a participant in the ESA’s Third Party Missions Program, meaning the ESA can sponsor the data delivery through their Earth

Observation User Services Portal.

To achieve ESA sponsorship of this data, a proposal was submitted including the objective of the project, researchers involved in the task, which satellite and product was being requested, and a general plan outlining the use of the sponsored data. Given the latency of proposal approval, and the seasonal characteristics of arctic sea ice, interim efforts were made to coincide freely available SN-2 10m resolution data with IS-2's altimetry.

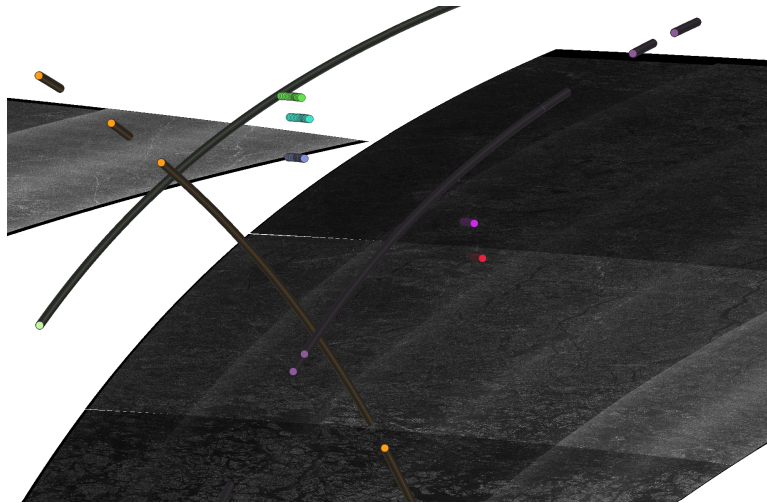


Figure 2.1: Near-Coincidence of SN-2 and IS-2, February 20-21 2023

Referring to ESA's Copernicus Open Access Hub and NASA's Earthdata Search tool, a near coincident set of SN-2 and IS-2 data was obtained for February 20-21 of 2023 (Figure 2.1). The SAR imaging clearly captured regions of arctic ice, and did so on February 20th at 4:50pm UTC. The predominantly spatially coincident IS-2 measurements, being the long purple and orange tracks in the figure, crossed the region at 10am and 10pm UTC on February 21. This data while immensely geographically coincident, was dubious because of its 17 and 29 hour respective temporal delay. Utility scripts were devised to track buoy movement in the area across the time period, and the nearest buoy (purple) to any of the tracks was 30 kilometers

away and had traveled another 8 km during the data's time difference. The corroboration of buoy movement in the area invalidates the possibility of the data being correlated, as it's unreasonable to account for the drift of the ice over the given time and space scale. While unsuccessful, this instance demonstrates the unavailability of naturally coincident data and the inefficiencies in obtaining it.

Later, the ESA approved the project proposal and agreed to sponsor 2 SPOT and 2 SLEA images. With this sponsorship, specific SAR imagery was then ordered that coincided with IS-2's flight path. In preparation for the data order, locations were selected in the ICESAT-2 mobile application and validated to have sea ice by viewing recent SN-2 data via Copernicus Open Access Hub. Then, an order form was submitted to ICEYE detailing the acquisition information to which they'd respond regarding its feasibility. This ordering and validation was repeated until all 4 sponsored images were fulfilled (Figure 2.2).

2.2 Laser Altimetry (IceSat-2)

The ICESAT-2 mobile application and ICEYE's flexibility handled the issues of spatial and temporal coincidence. IS-2 data was simply collected from the National Snow and Ice Data Center (NSIDC) repository after its own acquisition of the selected area. Each IS-2 acquisition offers multiple data products, but for the study of sea ice the ATL10 product is most relevant. The ATL10 data product contains inferences about sea-ice freeboard using data propagated from their ATL07 sea ice height product. Thus, a single ATL10 delivery contains the interpreted sea surface height, ice surface height, and the total freeboard [2] needed to infer sea ice thickness (Equation 1.1).

The recorded data is captured and delivered in a ".h5" file requiring

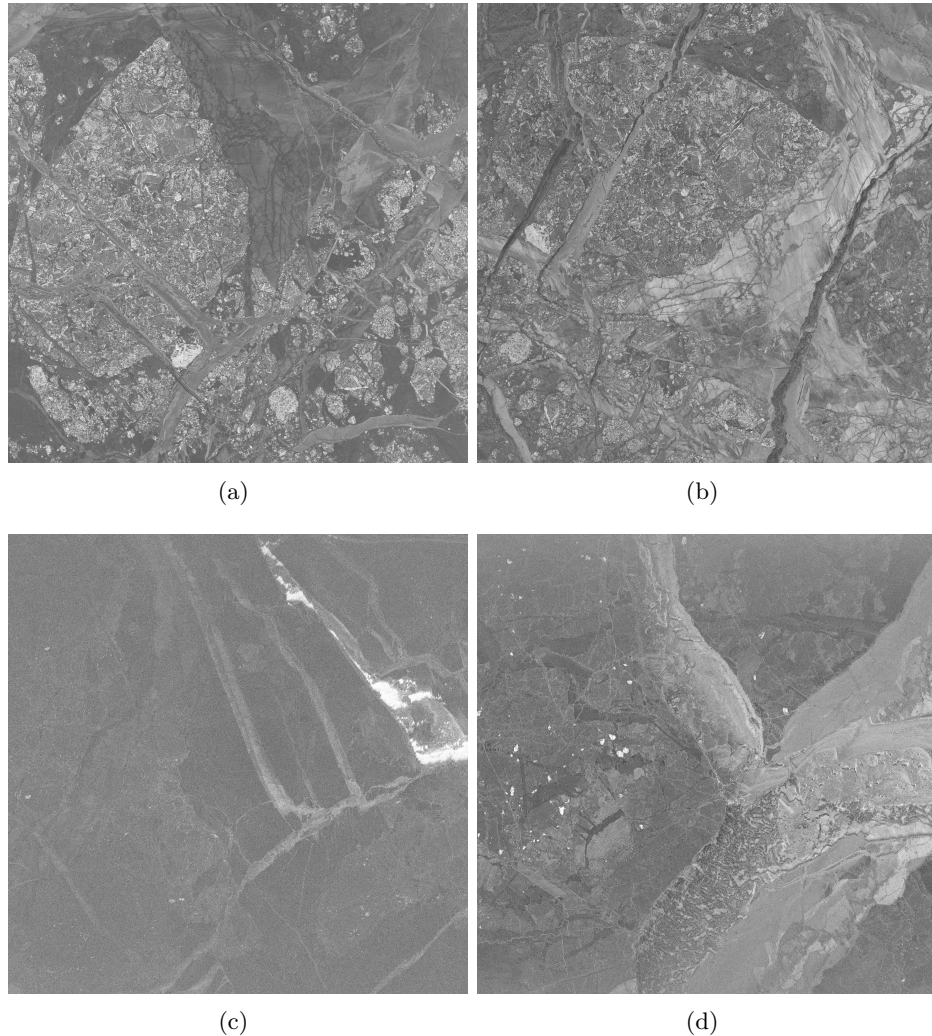


Figure 2.2:

- (a) SLEA 1/19 02:35:35 UTC (73.396, -141.668)
- (b) SLEA 1/19 04:40:35 UTC (73.395, -141.664),
- (c) SPOT 1/20 13:29:02 UTC (72.816, -133.975),
- (d) SPOT 1/20 20:25:52 UTC (72.816, -133.976)

parsing to extract relevant information. Appendix A contains a list of the fields that were extracted, and a brief description of each based upon the ATL10 data product specification [2].

After receiving the SAR imaging from ICEYE and the IS-2 data from the NSIDC, the best delivery in terms of coincidence was Figure 2.2(b).

Figure 2.2(b) was 6 minutes coincident with the IS-2 track, thus offering the greatest source of ground truth. A severe limitation of the extracted data though, is that IS-2 omits data when it detects ice concentration $<50\%$. For this reason, the ATL10 .h5 product for this acquisition only contained data from its GT2R and GT3R beams, effectively yielding 33% of the information initially expected. Figure 2.3 shows the intersecting IS-2 tracks, and figure 2.4 demonstrates the surface profile of the captured data, which will be used to interpolate ice thickness in future sections.

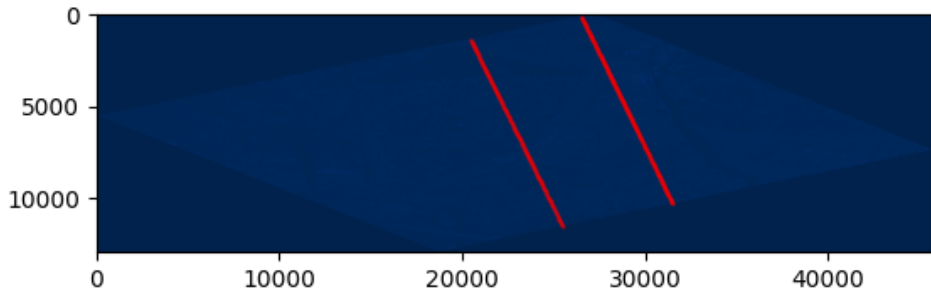


Figure 2.3: IS-2 Tracks across ICEYE Image

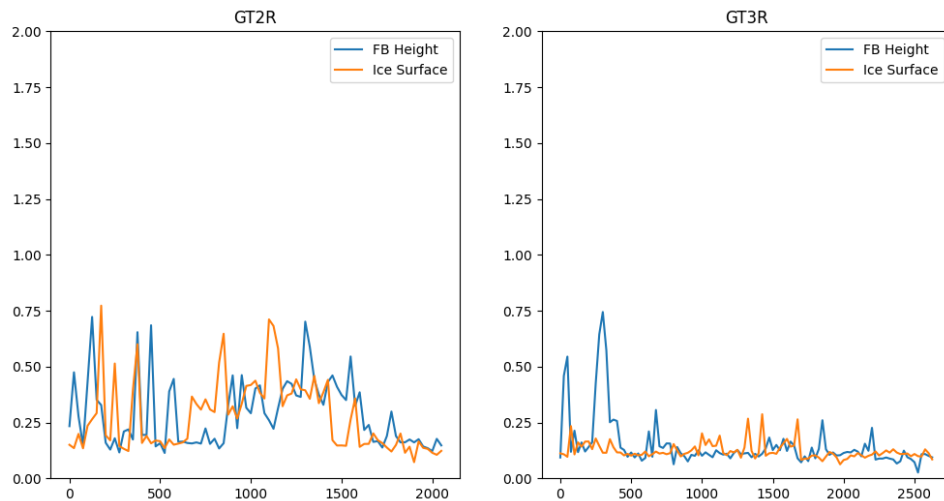


Figure 2.4: Ice Surface Profiles

Experimentation

The intuition behind developing a CNN on this dataset is novel. Many related works demonstrate the feasibility of using CNN models to classify or segment SAR imaging [10], but tend not to explore regression tasks. This could be a result of minimal data like the set derived for this study being accessible to the public. Furthermore, attempting to relate IS-2 footprints to high resolution SAR imaging involves deriving information from single-channel imagery of low pixel dimension. Compounded with the 33% yield of anticipated data from the ICEYE image, the limited data problem is exacerbated.

3.1 Setup

The coincident data is first extracted from the ICEYE imagery, yielding 4,683 17x17 tiles with associated LiDAR measurements. The selected densities used for interpolation are as follows, where the snow density is drawn from historical measurements during the month of January [11].

$$\begin{aligned}\rho_i &= \text{Density of sea ice } (916 \frac{kg}{m^3}) \\ \rho_s &= \text{Density of snow } (300 \frac{kg}{m^3}) \\ \rho_w &= \text{Density of water } (1024 \frac{kg}{m^3})\end{aligned}$$

Using Equation 1.1, each tile’s elevation readings are converted to their associated thickness. Some values of freeboard are negative, so they are interpreted to represent the absence of snow and an overestimate of sea ice surface elevation. The negative freeboard values are then added to the sea ice surface elevation to compensate. Each tile’s interpolated ice thickness can be visualized in Figure 3.1.

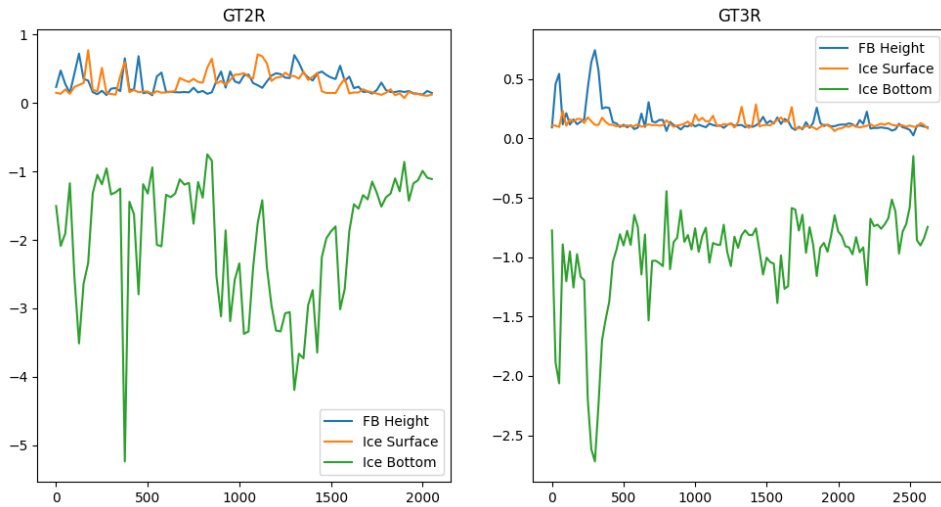


Figure 3.1: Interpolated Ice Thickness

The experimental model for the data is a feed forward neural network, consisting of 3 convolutional layers and 3 fully connected layers. Each convolutional layer is followed by the ReLU activation function, and the model uses the ADAM optimizer at a 10^{-5} learning rate based upon the L1 loss function. Given the already minimal pixel-space dimension, pooling and filter dilation are avoided to better preserve information across layers of the network.

The intuition behind experimenting with a simple model is rooted largely from the sparseness of existing studies attempting regression on low-resolution single channel images. Studies on classification, however, find that

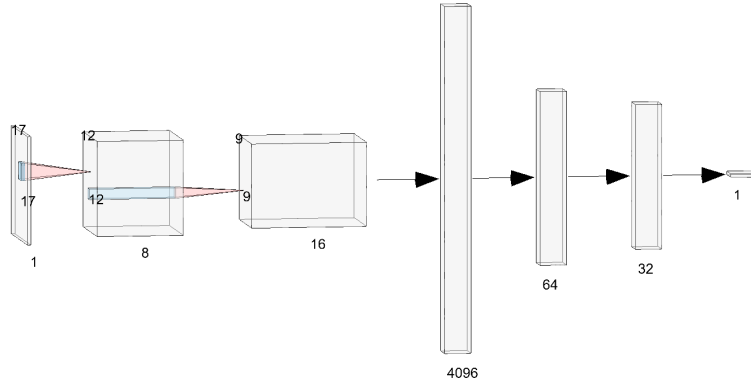


Figure 3.2: CNN Architecture

wider datasets (data that spans more classes) benefit from a larger amount of neurons in fully connected layers [14]. Regression tasks for continuous numbers can be thought of as infinite classification, thus supporting the decision to implement multiple fully connected layers of large dimension. Some classification studies find value in decreasing filter sizes with model depth [15], but for this model, kernel size is decreased from 5 to 3 only between the first and second convolution layer.

The training process for the model uses 80% of the data to train and 20% to test, a batch size of 32 to promote faster convergence, random flipping and rotation to prevent over-fitting, and scaling of each pixel to the [0,255] color range. The model is trained over 100 epochs.

3.2 Model Results

After 100 epochs, the model fails to converge (Figure 3.3). The L1 Loss function plateaus at ≈ 0.66 , and the model predicts a concentrated set of values slightly lower than the test set's mean. This value can be explained by the L1 Loss function's insensitivity towards outliers, as the mean (vertical bar) would be shifted right because of the skew in the input distribution.

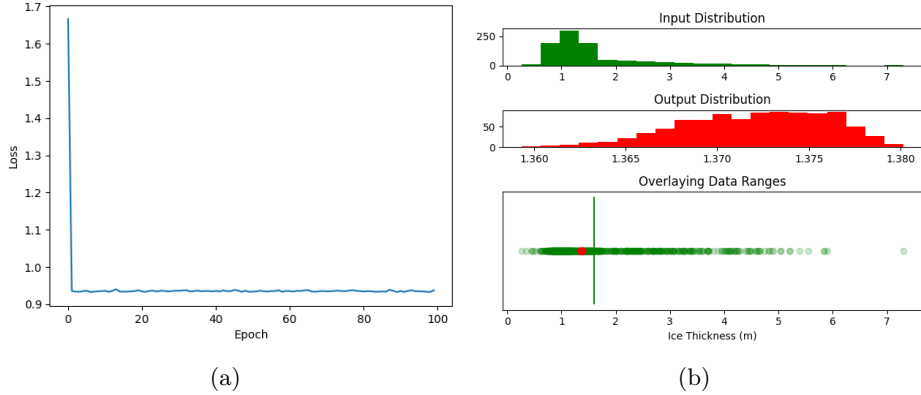


Figure 3.3: (a) Model Convergence (b) Model Predictions

The model reports an R2 value of -.056 and an RMSE of 0.9996, both of which suggest the model does not fit the data at all. The normalized RMSE is 0.14, which seemingly better, is only the result of the relatively narrow range of ice thicknesses being predicted in the testing set. Minor changes to the activation function and hyper-parameters yielded no significant difference to the model's evaluation metrics, nor did they assist in loss convergence. The inadequacies demonstrated by these tests suggest a more sophisticated architecture would be needed to better associate these low-resolution 1 channel images with their interpolated thickness measurements.

Discussion

While the approach to applying IS-2’s LiDAR measurements to ICEYE’s SAR imaging was intuitive, there are several limitations of the experiment that should be acknowledged. These can be split into technical and conceptual limitations, where the former is responsible for immediate flaws in experimentation, and the latter can be viewed as persistent by nature of how they are related to the task. The practical implications of a working model are discussed after the limitations, and the section is concluded by future works for this project.

4.1 Technical Limitations

Limitations of the experimentation range from the data collection to the architecture and testing configuration. Firstly, the model’s failure to converge was likely the result of inadequate architecture, but the restricted amount of data itself was plausibly a second limiting factor. As discussed at the end of the Data Collection section, of the 4 sponsored images delivered from ICEYE, only (Figure 2.2(b)) appeared to be correlated closely enough with IS-2’s track to be considered ground truth. Despite efforts to validate the location and concentration of sea ice in the acquisition area by using Copernicus Access Hub, the selected area was too sparse for IS-2 to deliver information from all 6 beams. The low resolution of SN-2 data via Copernicus

Access Hub combined with the latency between the data order and delivery means that there is a degree of randomness with any data acquisition even when sponsored. IS-2's data delivery flagged 70% of its gathered data for the possible interference of weather, either through blowing snow or clouds. Considering IS-2's weather flag then, the original expectation of $\approx 11,300$ tiles from the 2 SPOT and 2 SLEA images actually only produced 1,391 tiles, for a yield of 12.30%.

Furthermore with the data, the coincidence of (Figure 2.2(b)) is based on the assumption that the ice did not drift more than 17 meters within the acquisition window. Essentially, if the ice drifted even $3 \frac{m}{min}$ it's possible for the data to be a close proxy for the ground truth, but technically incorrect altogether. Buoy data for the time frame showed that 2 buoys, 185km and 300km away were traveling at a mean speed of $12 \frac{m}{min}$ and $16.67 \frac{m}{min}$ respectively during the hour of acquisition. Combined with the assumed geolocation accuracy of 5m [3] and that some studies find the mean effective footprint of IS-2 to be $10.9 \pm 1.2m$ [16], the assumption of coincidence becomes weaker.

Statistically, many measurements used during the study were accompanied by uncertainties, standard deviations, and confidence levels. These values were ignored during the experimentation, but should be considered in more thorough analysis in the future.

4.2 Conceptual Limitations

The introduction discussed the assumption of hydrostatic equilibrium and associated Equation 1.1 as an established method to deduce ice thickness from remote measurements. Like previously mentioned, there is contention between which values to use for each density. Simply by assuming the

maximum and minimum of acceptable densities for sea ice and snow, the same data from the experimentation can be seen ranging over a whole meter in some places like index 1050 (Figure 4.1). It's important to realize that this exact acquisition saw freeboard $< 1\text{m}$, but with acquisitions of ice with more freeboard, these error bounds would increase in magnitude.

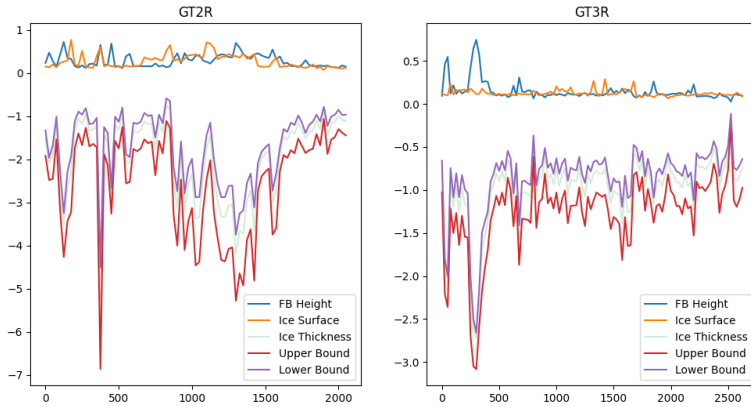


Figure 4.1: Bounded Ice Thickness

Coupled with the issue of ice density in the hydrostatic model, is the general assumption of ice homogeneity. Figure 1.1 demonstrates the densities involved in interpolating for sea thickness, but it's important to realize these forces are assumed to be at play on independent buoyant ice segments. In practicality, ice floes as a whole are in hydrostatic equilibrium and the point-to-point assumption used in Figure 1.1 does not necessarily hold [9]. The differences can be results of ice deformation or composition, ridges, or even internal shear forces [1], [8].

A final conceptual limitation with the corroboration of LiDAR with SAR imaging, is that the specific satellite capturing the image has a meaningful effect on the model being used. ICEYE's SAR imaging was pursued because of its high 1m resolution. However, these images were captured using X-Band frequencies which are different from SN-2's [5], [13] frequencies. One

of SAR's advantages is its ability to permeate through snow, allowing for it to capture the ice-surface below it. It's exact penetration depth though, is highly variable across the range RADAR [17]. In this sense, the tiles derived from ICEYE will have to be compared to other X-Band SAR imaging satellites to ensure both images represent the same context.

4.3 Practical Implications

The development of a model like this has practical implications in both science and navigation. By tracking the thickness of ice floes across the arctic and measuring how a single floe grows or melts over time, researchers can better model the dynamics of sea ice using quantifiable changes. In the field of navigation, singular SAR images can be used to determine regions of thick and thin ice and use the information to better plan routes through arctic passages.

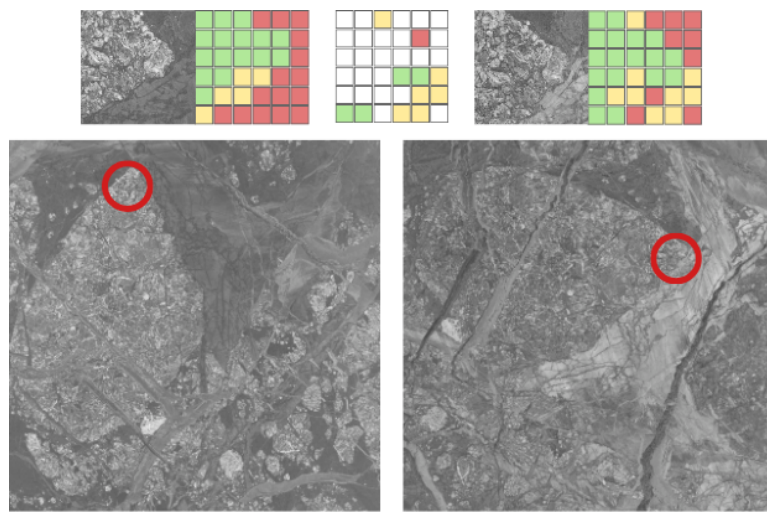


Figure 4.2: Change Detection between geo-located Figures 2.2(a) and 2.2(b)

4.4 Future Work

As mentioned in the experimentation, little work has been done in regression tasked CNNs of low resolution single channel images. The difficulty in aggregating a dataset for this study suggests that this task may not be a good use case for these deep learning models, as they rely heavily on mass amounts of data. However, the U-Net architecture is one such CNN that has seen efficacy in sea ice SAR imaging, particularly in image segmentation, and could be explored in its regression capabilites on lower-resolution images [10]. Moving forward, pursuing ensemble learning through a more statistical approach of the low resolution data would be a valuable use of the obtained data set, and possibly more feasible than a deep learning model.

Conclusion

Although this thesis did not yield a model capable of applying IceSat-2's precise LiDAR onto SAR imaging, it demonstrated the difficulty of acquiring and processing related remote sensing data sets. With substantial effort, satellite products can be coordinated to acquire data at nearly equivalent times and places. In the arctic, drifting ice further complicates data collection because ideal conditions rely on the intersection of satellite tracks with each other, and the steadiness of the sea ice. The captured data set of this thesis is rare in its coincidence of LiDAR and high resolution SAR imagery, but can not be validated by buoy movement to be completely accurate. More work will need to be done in modeling single channel, low resolution images before being able to map the small LiDAR footprints onto expansive SAR imaging. Accomplishing this task will drastically improve our understanding of arctic sea ice, which has implications both in science and navigation.

List of Figures

1.1	Historic In-Situ Data Availability in the Beaufort Sea Region	4
1.2	SAR Speckle Noise	6
1.3	Ice Thickness Isostatic Assumption	7
2.1	Existing Coincident Data Unavailability	10
2.2	ICEYE Captured SAR Imagery	12
2.3	Overlaid LiDAR and SAR Readings	13
2.4	Ice Surface Profile of Acquired Data	13
3.1	Interpolated Ice Thickness	15
3.2	CNN Architecture	16
3.3	Model Performance	17
4.1	Effect of Density Estimations on Ice Thickness Interpolation .	20
4.2	Implications of LiDAR mapped SAR	21

Bibliography

- [1] G. Timco and W. Weeks, “A review of the engineering properties of sea ice”, *Cold Regions Science and Technology*, vol. 60, no. 2, pp. 107–129, 2010, ISSN: 0165-232X. DOI: <https://doi.org/10.1016/j.coldregions.2009.10.003>. [Online]. Available: <https://www.sciencedirect.com/science/article/pii/S0165232X09001797>.
- [2] K. R., A. A. Petty, G. Cunningham, *et al.*, *Atlas/icesat-2 l3a sea ice freeboard, version 6*, 2023. DOI: 10.5067/ATLAS/ATL10.006. [Online]. Available: <https://nsidc.org/data/ATL10/versions/6>.
- [3] T. Schenk, B. Csatho, and T. Neumann, “Assessment of icesat-2’s horizontal accuracy using precisely surveyed terrains in mcmurdo dry valleys, antarctica”, *IEEE Transactions on Geoscience and Remote Sensing*, vol. 60, pp. 1–11, 2022. DOI: 10.1109/TGRS.2022.3147722.
- [4] P. Singh, M. Diwakar, A. Shankar, R. Shree, and M. Kumar, “A review on sar image and its despeckling”, *Archives of Computational Methods in Engineering*, vol. 28, no. 7, pp. 4633–4653, 2021, ISSN: 1886-1784. DOI: 10.1007/s11831-021-09548-z. [Online]. Available: <https://doi.org/10.1007/s11831-021-09548-z>.
- [5] C. D. S. Ecosystem, *Sentinel-2 — dataspace.copernicus.eu*, <https://dataspace.copernicus.eu/explore-data/data-collections/sentinel-data/sentinel-2>, [Accessed 09-04-2024].

- [6] H. Yang, J. Yu, Z. Li, and Z. Yu, “Non-local sar image despeckling based on sparse representation”, *Remote Sensing*, vol. 15, no. 18, 2023, ISSN: 2072-4292. DOI: 10.3390/rs15184485. [Online]. Available: <https://www.mdpi.com/2072-4292/15/18/4485>.
- [7] Petty, A. A., N. Kurtz, R. Kwok, T. Markus, and T. A. Neumann., *Icesat-2 l4 along-track sea ice thickness, version 1*, 2022. DOI: 10.5067/JTI5YG3S6VAJ. [Online]. Available: <https://nsidc.org/data/IS2SITDAT4/versions/1>.
- [8] J. K. Hutchings, P. Heil, O. Lecomte, R. Stevens, A. Steer, and J. L. Lieser, “Comparing methods of measuring sea-ice density in the east antarctic”, *Annals of Glaciology*, vol. 56, no. 69, 77–82, 2015. DOI: 10.3189/2015AoG69A814.
- [9] S. Forsström, S. Gerland, and C. A. Pedersen, “Thickness and density of snow-covered sea ice and hydrostatic equilibrium assumption from in situ measurements in fram strait, the barents sea and the svalbard coast”, *Annals of Glaciology*, vol. 52, no. 57, 261–270, 2011. DOI: 10.3189/172756411795931598.
- [10] Y. Huang, Y. Ren, and X. Li, “Classifying sea ice types from sar images using a u-net-based deep learning model”, in *2021 IEEE International Geoscience and Remote Sensing Symposium IGARSS*, 2021, pp. 3502–3505. DOI: 10.1109/IGARSS47720.2021.9554511.
- [11] S. G. Warren, I. G. Rigor, N. Untersteiner, *et al.*, “Snow depth on arctic sea ice”, *Journal of Climate*, vol. 12, no. 6, pp. 1814–1829, 1999.
- [12] *Sentinel-2 - Missions - Sentinel Online - Sentinel Online — sentinel.copernicus.eu*, <https://sentinels.copernicus.eu/web/sentinel/missions/sentinel-2>, [Accessed 11-04-2024].

- [13] *Types of SAR Data Products - ICEYE Product Documentation* — sar.iceye.com, <https://sar.iceye.com/5.2.5/>, [Accessed 12-04-2024].
- [14] S. S. Basha, S. R. Dubey, V. Pulabaigari, and S. Mukherjee, “Impact of fully connected layers on performance of convolutional neural networks for image classification”, *Neurocomputing*, vol. 378, pp. 112–119, 2020, ISSN: 0925-2312. DOI: <https://doi.org/10.1016/j.neucom.2019.10.008>. [Online]. Available: <https://www.sciencedirect.com/science/article/pii/S0925231219313803>.
- [15] A. Ganj, M. Ebadi, M. Darvish, and H. Bahador, *Lr-net: A block-based convolutional neural network for low-resolution image classification*, 2023. arXiv: 2207.09531 [cs.CV].
- [16] L. Magruder, K. Brunt, T. Neumann, B. Klotz, and M. Alonso, “Passive ground-based optical techniques for monitoring the on-orbit icesat-2 altimeter geolocation and footprint diameter”, *Earth and Space Science*, vol. 8, no. 10, e2020EA001414, 2021, e2020EA001414 2020EA001414. DOI: <https://doi.org/10.1029/2020EA001414>. eprint: <https://agupubs.onlinelibrary.wiley.com/doi/pdf/10.1029/2020EA001414>. [Online]. Available: <https://agupubs.onlinelibrary.wiley.com/doi/abs/10.1029/2020EA001414>.
- [17] R. Kwok, “Satellite remote sensing of sea-ice thickness and kinematics: A review”, *Journal of Glaciology*, vol. 56, no. 200, 1129–1140, 2010. DOI: [10.3189/002214311796406167](https://doi.org/10.3189/002214311796406167).

Appendix A: ATL10 Product

Field Name	Description
/freeboard_segment/latitude	ATL10 Data Product Columns
/freeboard_segment/longitude	ATL10 Data Product Columns
/freeboard_segment/beam_fb_height	ATL10 Data Product Columns
/freeboard_segment/beam_fb_confidence	ATL10 Data Product Columns
/freeboard_segment/beam_fb_quality	ATL10 Data Product Columns
/freeboard_segment/beam_fb_unc	ATL10 Data Product Columns
/freeboard_segment/beam_refsurf_ndx	ATL10 Data Product Columns
/freeboard_segment/height_segment_id	ATL10 Data Product Columns
freeboard_segment/seg_dist_x	ATL10 Data Product Columns
/freeboard_segment/heights/layer_flag	ATL10 Data Product Columns
/freeboard_segment/heights/ice_conc	ATL10 Data Product Columns
/freeboard_segment/heights/height_segment_1	ATL10 Data Product Columns
/freeboard_segment/heights/height_segment_2	ATL10 Data Product Columns
/freeboard_segment/heights/height_segment_3	ATL10 Data Product Columns
/freeboard_segment/heights/height_segment_4	ATL10 Data Product Columns
/freeboard_segment/heights/height_segment_5	ATL10 Data Product Columns
/reference_surface_section/beam_refsur	ATL10 Data Product Columns
/reference_surface_section/beam_refsur	ATL10 Data Product Columns
/reference_surface_section/beam_fb_unc	ATL10 Data Product Columns
/reference_surface_section/beam_refsur	ATL10 Data Product Columns
/reference_surface_section/beam_refsur	ATL10 Data Product Columns
/reference_surface_section/beam_refsur	ATL10 Data Product Columns